Inorganic Chemistry

Article

pubs.acs.org/IC

α-$Ag_{2-2x}Zn_xWO_4$ ($0 \le x \le 0.25$) Solid Solutions: Structure, Morphology, and Optical Properties

Paula F. S. Pereira,[†] Clayane C. Santos,[‡] Amanda F. Gouveia,[‡] Mateus M. Ferrer,[§] Ivo M. Pinatti,[‡] Gleice Botelho,[‡] Julio R. Sambrano,[§] Ieda L. V. Rosa,[‡] Juan Andrés,*[,∥] and Elson Longo[†]

[†]CDMF, LIEC, São Paulo State University, P.O. Box 355, Araraquara 14800-900, Brazil

[‡]CDMF, LIEC, Federal University of São Carlos, P.O. Box 676, São Carlos 13565-905, Brazil

[§]Modeling and Molecular Simulations Group, São Paulo State University, P.O. Box 473, Bauru 17033-360, Brazil

[∥]Department of Analytical and Physical Chemistry, University Jaume I, Castelló 12071, Spain

Supporting Information

ABSTRACT: A theoretical study was elaborated to support the experimental results of the Zn-doped α-Ag_2WO_4. Theses α-$Ag_{2-2x}Zn_xWO_4$ ($0 \le x \le 0.25$) solid solutions were obtained by coprecipitation method. X-ray diffraction data indicated that all α-$Ag_{2-2x}Zn_xWO_4$ ($0 \le x \le 0.25$) microcrystals presented an orthorhombic structure. The experimental values of the micro-Raman frequencies were in reasonable agreement with both previously reported and calculated results. Microscopy images showed that the replacement of Ag^+ by Zn^{2+} promoted a reduction in the average crystal size and modifications in the morphology, from rod-like with hexagonal shape to roll-like with a curved surface. A theoretical methodology based on the surfaces calculations and Wulff constructions was applied to study the particle shapes transformations and the surface energy variations in α-$Ag_{2-2x}Zn_xWO_4$ ($0 \le x \le 0.25$) system. The decrease in the band gap value (from 3.18 to 3.08 eV) and the red shift in photoluminescence with the Zn^{2+} addition were associated with intermediary energy levels between the valence and conduction bands. First-principles calculations with density functional theory associated with B3LYP hybrid functional were conducted. The calculated band structures revealed an indirect band gap for the α-$Ag_{2-2x}Zn_xWO_4$ models. The electronic properties of α-Ag_2WO_4 and α-$Ag_{2-2x}Zn_xWO_4$ microcrystals were linked to distortion effects and oxygen vacancies (V_O^x) present in the clusters, respectively. Finally, photoluminescence properties of α-Ag_2WO_4 and α-$Ag_{2-2x}Zn_xWO_4$ microcrystals were explained by means of distortional effects and oxygen vacancies (V_O^x) in [AgO_y] (y = 2, 4, 6, and 7) and [WO_6] clusters, respectively, causing a red shift. Calculations revealed that the substitution for Ag^+ with Zn^{2+} occurred randomly in the α-Ag_2WO_4 lattice, and it was more favorable on the Ag4 site, where the local coordination of Ag^+ cations was four.

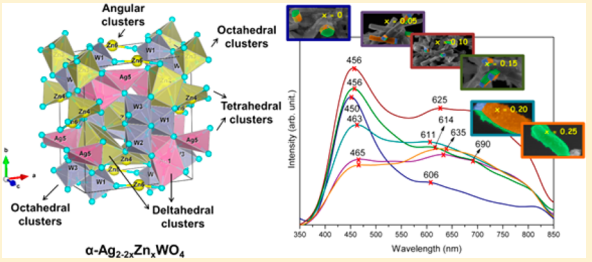

1. INTRODUCTION

Metal tungstates are a well-known family of inorganic materials due to their prominent properties with multifunctional applications in many fields such as catalysis, photocatalysis, microbial agents, and luminescence.[1−12]

α-Ag_2WO_4 is a significant member of this family, and a variety of particle characteristics and properties have been obtained using different methods such as electrochemical,[13] sonochemical,[3,14] supersonic assisted homogeneous precipitation,[15] conventional hydrothermal,[3] hydrothermal microwave,[5,16−21] and coprecipitation method.[3,4,16,22−30] Very recently, Fan et al. reported a preparation method for highly uniform one-dimensional α-Ag_2WO_4 nanostructures with a controllable aspect ratio.[31] α-Ag_2WO_4 has received significant attention owing to its potential applications, in different fields such as organic catalysis,[24,32,33] photocatalysis,[4,17,34] electrocatalysis,[25] gas sensing,[1,19] dye adsorbents,[14] photoswitches,[35] and as antimicrobial[5] and antibacterial agents.[14,15,17] These unique features provide the opportunity to tailor the basic physical and chemical properties and performance of α-Ag_2WO_4 compounds by intentionally mixing them with metals.

Obtaining solid solutions, formed by a mixture of two or more crystalline solids, is found to be a very effective strategy to tailor the crystal structure, continuous tenability of band gap values, and optical properties. Solid solutions may have new properties or improve on those existing in separate phases. In particular, the synthesis and formation mechanisms of the solid solutions of metal tungstate, their stability and corresponding properties, as well as the potential technological applications, are important topics of research.

In this context, the synthesis and characterization of solid solutions involving metal tungstates such as $Sr_{1-x}Pb_xWO_4$,[36] $Ca_{1-x}Sr_xWO_4$,[37] $Ba_{1-x}Sr_xWO_4$,[38] and $Sr_{1-x}Ba_xWO_4$[37] have been performed. The photoluminescence (PL) properties of $Ca_xSr_{1-x}WO_4$[39] and $Ca_{1-x}Cd_xWO_4$[40] have been analyzed,

Received: February 7, 2017

DOI: 10.1021/acs.inorgchem.7b00201
Inorg. Chem. XXXX, XXX, XXX−XXX

while the structures, optical properties, and magnetism have been studied for $Zn_{1-x}Ni_xWO_4$,[41] $Mn_{1-x}Cu_xWO_4$,[42] $Cd_{1-x}Zn_xWO_4$,[43] $Ni_{1-x}Co_xWO_4$,[44] $Zn_{1-x}Cu_xWO_4$,[45] and $Zn_{1-x}Co_xWO_4$.[46]

Our group is engaged in a research devoted to finding a rational synthesis of solid based on the α-Ag_2WO_4 material, and very recently, we performed a study on the effects of chemical substitution of α-$Ag_{2-2x}Ni_xWO_4$ solid solutions.[47] α-Ag_2WO_4 presents an orthorhombic structure with space group $Pn2n$. Each W cation is bonded to six oxygen atoms, while the Ag cations are found to have two-, four-, six-, and seven-coordinated geometries. Therefore, the corresponding building blocks of this structure are the $[WO_6]$ cluster with O_h symmetry and $[AgO_y]$ (y = 2, 4, 6, and 7) clusters with C_{2v}, T_d, O_h, and D_{5h} symmetries, respectively. These clusters are distorted, because different W−O and Ag−O distances can be sensed, and then these clusters present deviations from the ideal symmetry.[3,48] $ZnWO_4$ has a monoclinic structure with the space group $P2/c$, where six oxygen ions are arranged around W and Zn cations forming a distorted octahedral coordination, corresponding to $[WO_6]$ and $[ZnO_6]$ clusters, respectively.[49] In both α-Ag_2WO_4 and $ZnWO_4$ structures, all clusters are asymmetric and not homogeneous. This fact results in a set of nonequivalent clusters of metal−oxygen bonds distributed over the lattice. In addition, differences in the ionic radii and charges between Ag^+ and Zn^{2+} may produce lattice distortions and vacancies in the crystal. Thus, through the substitution of Ag^+ with Zn^{2+} in α-Ag_2WO_4, an interesting prospect for applications is the control of material properties in the corresponding solid solution by disturbance of the local M−O environment.

Herein, we developed new α-$Ag_{2-2x}Zn_xWO_4$ ($0 \le x \le 0.25$) solid solutions via a simple coprecipitation (CP) method. The structure was confirmed by X-ray diffraction (XRD), X-ray fluorescence spectrometry (XRF), Rietveld refinement data, and micro-Raman (MR) and Fourier transform infrared (FTIR) spectroscopies. The optical properties were investigated by ultraviolet−visible (UV−vis) diffuse reflectance spectroscopy and photoluminescence (PL). Field-emission scanning electron microscopy (FE-SEM) images were employed to evaluate the shapes, sizes, and growth processes of the crystals as the doped concentration of Zn^{2+} ions in the α-Ag_2WO_4 network was increased. To complement these experimental results, theoretical calculations with the density functional theory (DFT) were performed. The electronic information, such as band structure and density of states (DOS), and Raman spectra were calculated to understand the phenomenon of structural order−disorder in the α-Ag_2WO_4 structure caused by Zn^{2+} replacement.

The paper is organized in three other sections. Section 2 describes the methodology details. Section 3 exposes the results and the discussion concerning the structural and properties characteristics. The paper combined experimental and theoretical results in order to understand the relationship between the structural modifications and the obtained PL properties. Section 4 describes our conclusions.

2. EXPERIMENTAL SECTION

Synthesis of α-$Ag_{2-2x}Zn_xWO_4$ Microcrystals. The α-$Ag_{2-2x}Zn_xWO_4$ (x = 0, 0.05, 0.10, 0.15, 0.20 and 0.25) microcrystals were prepared by the CP method. The procedure for the typical α-$Ag_{2-2x}Zn_xWO_4$ microcrystals synthesized by the CP method is described as follows: 1×10^{-3} mol of tungstate (VI) sodium dihydrated ($Na_2WO_4{\cdot}2H_2O$; 99.5% purity, Sigma-Aldrich) and 2×10^{-3} mol of silver(I) nitrate ($AgNO_3$; 99.8% purity, Sigma-Aldrich) were dissolved separately in 50 mL of deionized water at 80 °C under magnetic stirring. The solution with Ag^+ and NO_3^- was added to the solution containing the WO_4^{2-} ions, and this solution remained at 80 °C under magnetic stirring for 30 min. After that, a yellow suspension appeared, and a white precipitate was rapidly formed. The solid solutions were prepared according to the molar ratio in α-$Ag_{2-2x}Zn_xWO_4$ (x = 0.05, 0.10, 0.15, 0.20, and 0.25) considering the charge balance between Ag^+ and Zn^{2+}. Zinc nitrate octahydrated ($Zn(NO_3)_2{\cdot}8H_2O$; 99.99% purity, Sigma-Aldrich) was added to $AgNO_3$ solution, and the procedure was similar to that described for the α-Ag_2WO_4. The resulting suspensions were washed several times with deionized water to remove the residual Na^+ ions. The crystalline α-$Ag_{2-2x}Zn_xWO_4$ microcrystals were collected and dried in an oven at 70 °C.

Characterization. These α-$Ag_{2-2x}Zn_xWO_4$ microcrystals were structurally characterized by XRD patterns using a D/Max-2000PC diffractometer Rigaku (Japan) with Cu Ka radiation (λ = 1.5406 Å) in the 2θ range from 10° to 70° in the normal routine with a scanning velocity of 2°/min and from 10° to 110° with a scanning velocity of 1°/min in the Rietveld routine. XRF analyses were performed on a Shimadzu EDX 720 XRF spectrometer. MR spectroscopy was conducted on a Horiba Jobin-Yvon (Japan) spectrometer charge-coupled device detector and argon-ion laser (Melles Griot, United States) operating at 514.5 nm with maximum power of 200 mW. The spectra were measured in the range of 250−1000 cm^{-1}. FTIR spectroscopy was recorded in the range from 250 to 1000 cm^{-1} using KBr pellets as a reference in a Bomem−Michelson spectrophotometer in transmittance mode (model MB102). The shapes and sizes of these α-$Ag_{2-2x}Zn_xWO_4$ microcrystals were observed with an FE-SEM Inspect F50 (FEI Company, Hillsboro, OR) operated at 5 kV. The optical properties of the α-$Ag_{2-2x}Zn_xWO_4$ microcrystals were analyzed by UV−vis and PL spectroscopies. UV−vis spectra were taken using a (Varian, USA) spectrophotometer (model Cary 5G) in a diffuse-reflectance mode. PL measurements were performed through a Monospec 27 monochromator (Thermal Jarrel Ash) coupled to a R446 photomultiplier (Hamamatsu Photonics, Japan). A krypton-ion laser (Coherent Innova 90K; λ = 350.7 nm) was used as the excitation source; its maximum output power was maintained at 500 mW. The laser beam was passed through an optical chopper, and its maximum power on the sample was maintained at 40 mW. PL measurements were performed at room temperature.

Computational Details. All theoretical calculations for the α-Ag_2WO_4 and α-$Ag_{2-2x}Zn_xWO_4$ structure were performed with the CRYSTAL14 software package.[50] This code uses a Gaussian-type basis set to represent crystalline orbitals as a linear combination of Bloch functions defined in terms of local functions (atomic orbitals). The computational method is based in the DFT associated with the Becke's three-parameter hybrid nonlocal exchange functional[51] combinated with a Lee−Yang−Parr gradient-corrected correlation functional[52] (B3LYP). The diagonalization of the Fock matrix was performed using a (4 × 4 × 4) Pack-Monkhorst k-points grid in the reciprocal-space. The thresholds controlling the accuracy of the calculation of the Coulomb and exchange integrals were set to 1×10^{-8} and 1×10^{-14}, and the percent of Fock/Kohn−Sham matrix mixing was set to 30 (IPMIX keyword). The lattice parameters and the internal atomic coordinates were fully optimized until all force components were less than 1×10^{-6} eV $Å^{-2}$. The basis sets to describe the atomic centers of α-Ag_2WO_4 were the same as those employed by Longo et al.;[5] Zn atoms were described by 86−411d31G, which was obtained from the Crystal Web site.[53] The Raman vibrational modes and their corresponding frequencies were calculated using numerical second derivatives of total energies as implemented in the CRYSTAL14 package.[50] The band structure and DOS of the models were constructed along the appropriate high-symmetry directions of the corresponding irreducible Brillouin zone. Three models were constructed to more accurately describe structural and electronic properties derived from the experimental synthesis, a pure α-Ag_2WO_4, and two models in which the Zn^{2+} cation substitutes the Ag^+ cation

DOI: 10.1021/acs.inorgchem.7b00201
Inorg. Chem. XXXX, XXX, XXX−XXX

with formation of Ag vacancy, to consider the charge balance between Ag^{+} and Zn^{2+} cations. To evaluate the stability of substituted structures, we directly compared the total energies of the Zn replacement in the α-Ag_2WO_4. The procedure to obtain the complete set of morphologies, based on the Wulff construction, has been previously presented by Andrés et al.[54]

3. RESULTS AND DISCUSSION

XRD and XRF. The long-range order of α-$Ag_{2-2x}Zn_xWO_4$ was evaluated by XRD diffraction. Figure 1a–f shows the XRD patterns of the α-$Ag_{2-2x}Zn_xWO_4$ microcrystals, where x = 0.0, 0.05, 0.10, 0.15, 0.20, and 0.25, respectively, obtained by the CP at 80 °C for 30 min.

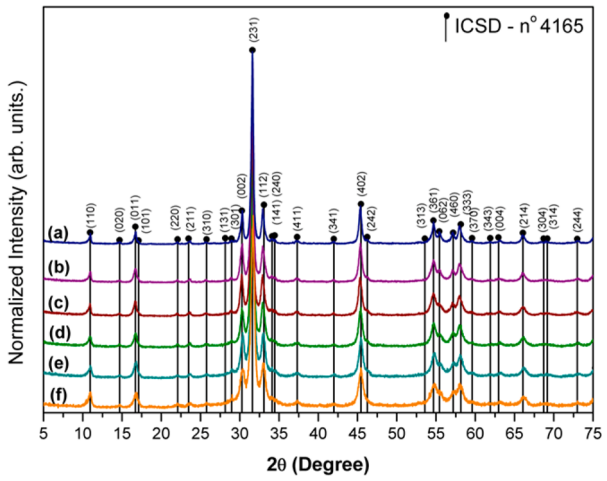

Figure 1. XRD of the α-$Ag_{2-2x}Zn_xWO_4$ (where x = (a) 0, (b) 0.05, (c) 0.10, (d) 0.15, (e) 0.20, and (f) 0.25) microcrystals obtained by the CP method at 80 °C for 30 min.

The XRD patterns (Figure 1) confirm that all α-$Ag_{2-2x}Zn_xWO_4$ samples have a pure orthorhombic structure (space group $Pn2n$, C_{2v}^{10} symmetry)[55,56] in accordance with the Inorganic Crystal Structure Database card No. 4165. The well-defined diffraction peaks of Figure 1 suggest a high degree of crystallinity,[57] for all materials. It is noticed that the orthorhombic periodicity was not affected by the presence of Zn^{2+} ions (see Figure 1b–f). The presence of Zn^{2+} in the lattice causes only a small structural distortion, confirmed by the lower definition of the diffraction peaks and the small shift observed in the strongest diffraction peaks of Figure SI-1. However, the diffraction peaks were slightly shifted to higher 2θ values as the Zn^{2+} ion concentration was increased, resulting in smaller interplanar distances. The left shift observed in some peaks of the x = 0.10 sample is possibly because the creation of homogeneous defects induced by the relaxation of the structure is reason for the number of vacancies and the kinds of sites occupied by the Zn atoms. The XRD results (Figure 1) indicate that the Zn^{2+} ions have been incorporated into the lattice and induced a slight reduction in the unit cell volume. It is important to note that the x = 0.25 is the maximum Zn-doping value, because from a large value of x the network α-Ag_2WO_4 is not maintained and even appears the formation of other phases (see Figure SI-2).

The presence of Zn^{2+} ions and their relative values in comparison with the Ag^{1+} were confirmed by XRF analysis (see Table SI-1). This methodology was used for the determination of silver and zinc concentrations in the α-$Ag_{2-2x}Zn_xWO_4$ structure by direct nondestructive method. The results show that the molar amounts were close to the calculated values for the syntheses. Some small deviations observed between theoretical and experimental values are assigned to matrix effects and equipment errors, such as calibration curve and interference effects.

Rietveld Refinement Analysis. A detailed study of the XRD patterns was conducted by means of Rietveld refinement analysis using the General Structure Analysis System (GSAS) program.[58] This technique allows an estimation of real structure parameters comparing the XRD peak profiles with the profile of other reported papers.[59] In these analyses, the background was refined using a Chebyshev polynomial of the first kind, and the peak profiles were adjusted by the Thompson-Cox-Hastings pseudo-Voigt (pV–TCH)[60] function with the asymmetry function described by Finger et al.[61] The anisotropy in half-width was taken into account using the model developed by Stephens.[62]

In this paper, we performed the Rietveld refinement to check the effects of the substitution of Ag^{+} by Zn^{2+} in the crystalline structure of α-$AgWO_4$. Rietveld refinement plots of α-$Ag_{2-2x}Zn_xWO_4$ for (a–f) x = 0, 0.05, 0.10, 0.15, 0.20, and 0.25, respectively, are shown in Figure SI-3. The Rietveld results were in accordance with ICSD Card No. 4165.[55] The crystals exhibited a single phase, confirming that there is a substitution for Ag^{+} by Zn^{2+} cations in all samples (x = 0.05, 0.10, 0.15, 0.20, and 0.25). Figure SI-3a–f shows good concordance between the experimental XRD patterns and theoretical results. This affirmation is based on the slight differences between the experimental intensity (Y_{Obs}) and the calculated intensity (Y_{Calc}), as shown by the line $Y_{Obs} - Y_{Calc}$. So, the quality of the refinement is generally checked using R-values (R_{wp}, R_{Bragg}, R_p, and χ^2). The Table SI-2 shows low deviations in the R-values, suggesting that the refinement result presents acceptable values. Additional information concerning the refinement reliability and the cell information are illustrated in Table SI-2. On the basis of the Rietveld refinement, there is a small difference between the unit cell parameters of each sample. The volume of the unit cell decreased with the Zn^{2+} incorporation; this is a consequence of the decrease in the cell parameters (see Table SI-2). Therefore, the substitution process of Ag^{+} by Zn^{2+} provokes a rearrangement of the geometry for the $[AgO_y]$ by $[ZnO_y]$ (y = 2, 4, 6, and 7) clusters; then, the local geometry of the metals (W, Ag, and Zn) and their corresponding interactions with oxygen anions contribute to the structural and electronic modifications.

Tables SI-3 and SI-4 shows the atomic positions for Ag, W, O, and Zn estimated in the refinement. These results show that there are changes in the positions of all atoms (Ag, W, and O), even with the introduction of a low Zn^{2+} concentration. These variations are more pronounced in the O positions, since they are the lighter atoms and form connections between the adjacent clusters along the $[AgO_y]$–$[ZnO_y]$ (y = 2, 4, 6, and 7) framework.

Unit Cell Representation for α-$Ag_{2-2x}Zn_xWO_4$. Figure 2 displays a schematic representation of the α-$Ag_{1.50}Zn_{0.25}WO_4$ orthorhombic unit cell. This structure was modeled using the Visualization for Electronic and Structural Analysis (VESTA) program.[63] From the lattice parameters and atomic coordinates obtained through of the Rietveld refinements (listed in Table SI-4), it was possible to construct the unit cell represented in Figure 2.

DOI: 10.1021/acs.inorgchem.7b00201
Inorg. Chem. XXXX, XXX, XXX–XXX

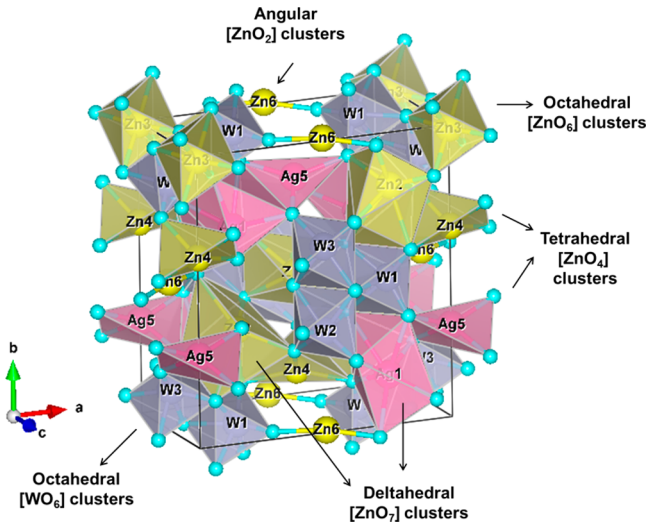

Figure 2. Schematic representation of crystalline units cells of α-$Ag_{2-2x}Zn_xWO_4$ (x = 0.25) microcrystals.

It is well-known[3,23,47] that α-Ag_2WO_4 is composed of three different W sites (W1, W2, and W3), all coordinated with six oxygen atoms forming a distorted [WO_6] cluster with an octahedral configuration. Six types of Ag sites with four different coordinations are presented (see Table 1): the Ag1 and Ag2 atoms are bonded with seven oxygen atoms generating a distorted bipyramidal [AgO_7] clusters; already the Ag3 atoms are linked by six oxygen atoms that form the distorted octahedral [AgO_6] cluster; for Ag4 and Ag5 atoms are arranged with four oxygen atoms, forming the distorted tetrahedral [AgO_4] clusters; and finally the Ag6 atoms are coordinated by two oxygen atoms, which form an angular [AgO_2] cluster.

The Rietveld refinement technique allows for identifying possible sites of Zn^{2+} cation occupancies in the α-$Ag_{2-2x}Zn_xWO_4$ lattice. The substitution of Ag sites with Zn^{2+} cations represented through [AgO_y]/[ZnO_y] (y = 2, 4, 6, and 7) clusters was determined for α-$Ag_{2-2x}Zn_xWO_4$ (x = 0.10, 0.15, 0.20, and 0.25) solid solutions, and these are listed in Table 1 with their atomic occupation values.

The refinement results show that the Zn^{2+} cations occupy different sites in the α-Ag_2WO_4 lattice. In the α-$Ag_{2-2x}Zn_xWO_4$ (x = 0.10 and 0.15) samples, Zn cations occupy the Ag1 and Ag2 sites corresponding to [AgO_7] and Ag6 sites of the [AgO_2] clusters. For α-$Ag_{2-2x}Zn_xWO_4$ (x = 0.20), the replacement takes place at these sites, as well as at the Ag4 site of the [AgO_4] cluster. Finally, for α-$Ag_{2-2x}Zn_xWO_4$ (x = 0.25), the substitutions occur in the Ag1, Ag2, Ag3, Ag4, and Ag6 sites of the [AgO_y] (y = 7, 7, 6, 4, and 2) clusters, respectively. With the increase in the amount of Zn^{2+}, there is a saturation of the substitution of Ag1, Ag2, and Ag6 sites, and the Zn^{2+} begins to occupy other sites—first the Ag4 and then the Ag3 sites. The [ZnO_y] (y = 7, 6, 4, and 2) arrangements are represented, respectively, by distorted bipyramidal, tetrahedral, octahedral, and angular clusters. The random occupations of the Zn^{2+} cations lead to distortions in the α-Ag_2WO_4 lattice observed by the different values of bond lengths and angles. These structural differences result in electronic order−disorder effects that, consequently, influence the α-Ag_2WO_4 material as a whole, which is confirmed mainly by the morphology and optical properties.

The atomic Zn occupation values are illustrated in Table 1; however, to have greater accuracy of these values, another technique such as extended X-ray absorption fine structure (EXAFS) analysis is required.

Structural Theoretical Analysis for α-$Ag_{2-2x}Zn_xWO_4$. The Rietveld results show that orthorhombic α-Ag_2WO_4 presents a very complex structure with different kinds of [AgO_y] clusters (where y can be 2, 4, 6, and 7) and that Zn^{2+} replacement can occur in any of these sites, depending on the Zn^{2+} concentration. To complement the experimental results and to study the effects of the presence of Zn^{2+} in the α-Ag_2WO_4 structure, two theoretical models, namely, A and B, for x = 0.25 (stoichiometry coefficient) of Zn ions were selected, in which the Zn replacements and Ag vacancies were made considering the charge balance between the Ag^+ and Zn^{2+} cations. In model A, the Ag2 sites were replaced by Zn^{2+} cations, while in model B, the replacement was on the Ag4 sites, and the vacancies were allocated near the substitution sites in both models.

The theoretical results indicated that the Zn^{2+} could be located in both Ag2 and Ag4 positions. However, the Zn replacement on the Ag4 site (model B) was 0.15 eV more stable than that in the Ag2 site (model A). The α-$Ag_{2-2x}Zn_xWO_4$ geometry showing the Zn additions and the Ag vacancy positions is depicted in Figure SI-4.

An analysis of the changes provoked by the substitution by Zn reveals that all clusters undergo modifications, exhibiting new coordination numbers and oxygen vacancies, as summarized in Table 2.

Table 2. Kinds of Clusters Present in the Models after Optimization

structures	Ag clusters	Zn clusters	W clusters
α-Ag_2WO_4	[AgO_7] [AgO_6] [AgO_4] [AgO_2]		[WO_6]
$ZnWO_4$		[ZnO_6]	[WO_6]
model A	[AgO_6] [AgO_5] [AgO_4]	[ZnO_4]	[WO_4]
model B	[AgO_5] [AgO_4]	[ZnO_4]	[WO_5] [WO_4]

Besides the structural distortion, the Zn replacement changes the α-Ag_2WO_4 electronic structure with the creation of holes in the systems, which are responsible for changes in the electronic properties of the tungstate. Thus, the properties are not only functions of the shallow defects (distorted clusters), as in the

Table 1. Atomic Zn Occupation in Sites of [AgO_y][a] Clusters of the α-$Ag_{2-2x}Zn_xWO_4$[b] Microcrystals

refined formula (α-$Ag_{2-2x}Zn_xWO_4$)	Ag1 [AgO_7]	Ag2 [AgO_7]	Ag3 [AgO_6]	Ag4 [AgO_4]	Ag5 [AgO_4]	Ag6 [AgO_2]
x = 0.10 occupation	[ZnO_7] 0.026	[ZnO_7] 0.046				[ZnO_2] 0.028
x = 0.15 occupation	[ZnO_7] 0.031	[ZnO_7] 0.058				[ZnO_2] 0.062
x = 0.20 occupation	[ZnO_7] 0.015	[ZnO_7] 0.087		[ZnO_4] 0.063		[ZnO_2] 0.035
x = 0.25 occupation	[ZnO_7] 0.022	[ZnO_7] 0.078	[ZnO_6] 0.022	[ZnO_4] 0.074		[ZnO_2] 0.048

[a] y = 2, 4, 6, and 7. [b] x = 0.10, 0.15, 0.20, and 0.25.

DOI: 10.1021/acs.inorgchem.7b00201
Inorg. Chem. XXXX, XXX, XXX−XXX

case of the α-Ag_2WO_4 structure, but also are functions of deeper defects (oxygen vacancies, V_O^x) in the clusters presented in α-$Ag_{2-2x}Zn_xWO_4$ caused by the rearrangement of the oxygen atoms around the cations. Therefore, in the α-$Ag_{2-2x}Zn_xWO_4$ solid solutions, there are $[WO_5 \cdot V_O^x]$, $[WO_4 \cdot 2V_O^x]$, $[ZnO_5 \cdot V_O^x]$, $[ZnO_4 \cdot 2V_O^x]$, and $[AgO_x]_d^x$ distorted clusters that are responsible for the PL properties.

Micro-Raman Spectroscopy Analysis. Through the Raman it is possible to determine the structural order of the material.[64] In accordance with the literature[65] the α-Ag_2WO_4 structure is classified into the internal and external modes, due to the weak coupling among group $[WO_4]^{2-}$ and the Ag^+ ion.[66] Thus, the internal modes are related to the vibrational molecular units, where the centers of mass remains immobile and the external mode refer to the lattice phonon, which is attributed to the motion of Ag^+ ion.[67]

Figure 3a illustrates the Raman spectra of α-$Ag_{2-2x}Zn_xWO_4$ (x = 0, 0.05, 0.10, 0.15, 0.20, and 0.25) microcrystals prepared at 80 °C for 30 min by the CP method, and Figure 3b compares the experimental Raman vibrational modes of α-$Ag_{2-2x}Zn_xWO_4$ microcrystals with the Raman-active modes calculated theoretically.

In Table SI-5, a comparison is presented among the experimental and simulated Raman active modes of α-Ag_2WO_4 microcrystals and values reported in the literature.[22,23,56,68]

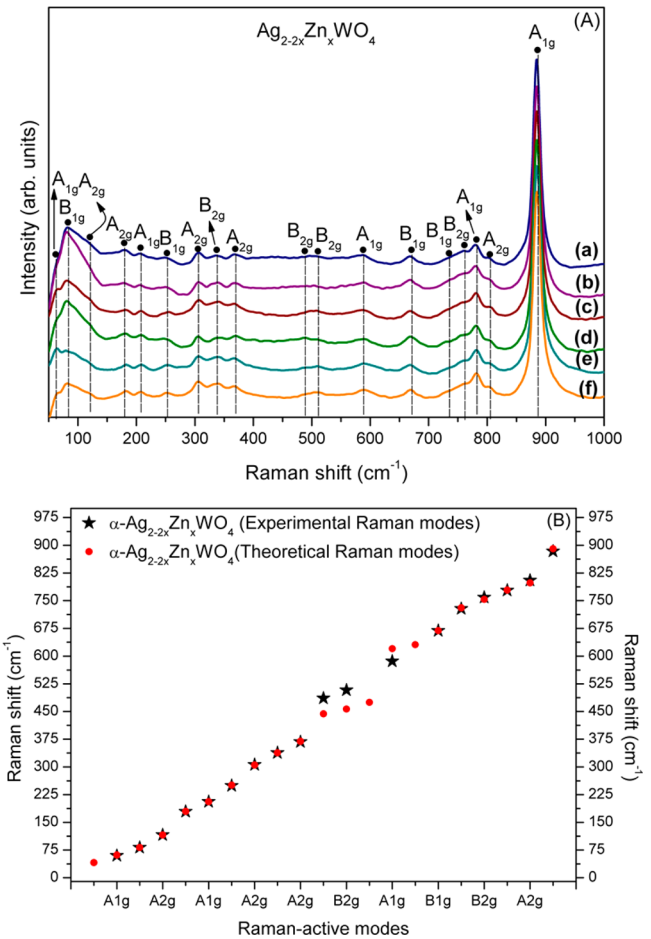

Figure 3. (a) Raman spectra of the α-$Ag_{2-2x}Zn_xWO_4$ (x = (a) 0, (b) 0.05, (c) 0.10, (d) 0.15, (e) 0.20, and (f) 0.25) microcrystals obtained by the CP method at 80 °C for 30 min and (b) comparison between the relative positions of theoretical and experimental Raman-active modes of α-$Ag_{2-2x}Zn_xWO_4$ microcrystals.

According to the literature,[56] there are 21 different vibrational modes in the tungstate with an orthorhombic structure. However, as can be seen in Figure 3a, 18 well-defined Raman-active modes were detected. These modes can be associated with the symmetric and asymmetric stretching among O−W−O moieties inside the $[WO_6]$ cluster, revealing peaks corresponding to the Raman-active internal modes A_1, A_2, B_1, and B_2,[5] while the modes located at lower energy represent the torsion among W−O and Ag−O situated in the 50−1000 cm^{-1} range. All modes presented in Figure 3a are intense and well-defined, suggesting that all α-$Ag_{2-2x}Zn_xWO_4$ (x = 0, 0.05, 0.10, 0.15, 0.20, and 0.25) microcrystals are structurally ordered at short-range. However, it is important to note that several modes were not observed probably due to their small intensities.

In this work, the active mode located in lower energy corresponds to translational A_{1g} (60 cm^{-1}) mode, and this refers to external or lattice phonons due to the Ag^+ heavy-cation movement in the rigid molecular unit. The strong interaction between the ions can cause an increase in the Raman-active mode intensity, and this occurs due to stretching and bending vibrations of shorter M−O bonds.[69] Thus, the intense peak at 884 cm^{-1} is attributed to the A_{1g} mode caused by the symmetric stretching vibrations of $[O \leftarrow W \rightarrow O]$ bonds of octahedral $[WO_6]$ clusters,[5,23] as opposed to the lattice modifier assigned to $[AgO_y]$ (y = 2, 4, 6, and 7) clusters. Three Raman modes (A_{1g}, B_{2g}, and B_{1g}) were also not observed, probably due to their small intensities.

Figure 3a displays that the Raman spectra for these samples presented a small change, indicating that the addition of Zn^{2+} ions in α-Ag_2WO_4 does not cause drastic changes in the stretching, torsional, and bending vibrational modes of the orthorhombic structure. It occurs because of the Zn^{2+} substitutes the Ag^+ cation; however, some variations were expected. For example, the intense peaks at ~884 cm^{-1} show reductions in their intensities as the Zn^{2+} concentration is increased (see Figure 3a), due to structural distortions in the α-$Ag_{2-2x}Zn_xWO_4$ microcrystal lattice produced by the Zn^{2+} substitution on the Ag^+ sites. These distortions also provoke changes in the bond lengths of the W−O distances in the $[WO_6]$ clusters.[23] The result is in accordance with the Rietveld data, where a decrease in the cell volume as the concentration of Zn^{2+} was increased in the α-Ag_2WO_4 lattice was observed.

One way to assess the quality of the theoretical models is to compare the vibrational modes. Figure 3b displays the Raman modes of the experimental samples, represented by (●), compared with our theoretical model (model B), illustrated as (*). Both experimental and theoretical results are in accordance with the literature[5,20,22,23,56] (see Table SI-5). This fact indicates that our model provides an appropriate representation of the α-$Ag_{2-2x}Zn_xWO_4$ solid solutions. A slight variation of some modes can be detected, mainly at 443.9, 456.7, and 474.9 cm^{-1} (B_g), which are associated with the stretching and bending vibrational modes of the Zn−O when compared with the experimental Raman modes (see Figure 3b and Table SI-5). This difference can be attributed to the different methods of synthesis, crystal size, and structural changes of bond distances Ag−O, W−O, and Zn−O, and bond angles Ag−W−O, Ag−W−Zn, along the $[AgO_y]-[WO_6]-[AgO_y]$ and $[AgO_y]-[WO_6]-[ZnO_y]$ (y = 2, 4, 6, and 7)[20] frameworks.

DOI: 10.1021/acs.inorgchem.7b00201
Inorg. Chem. XXXX, XXX, XXX−XXX

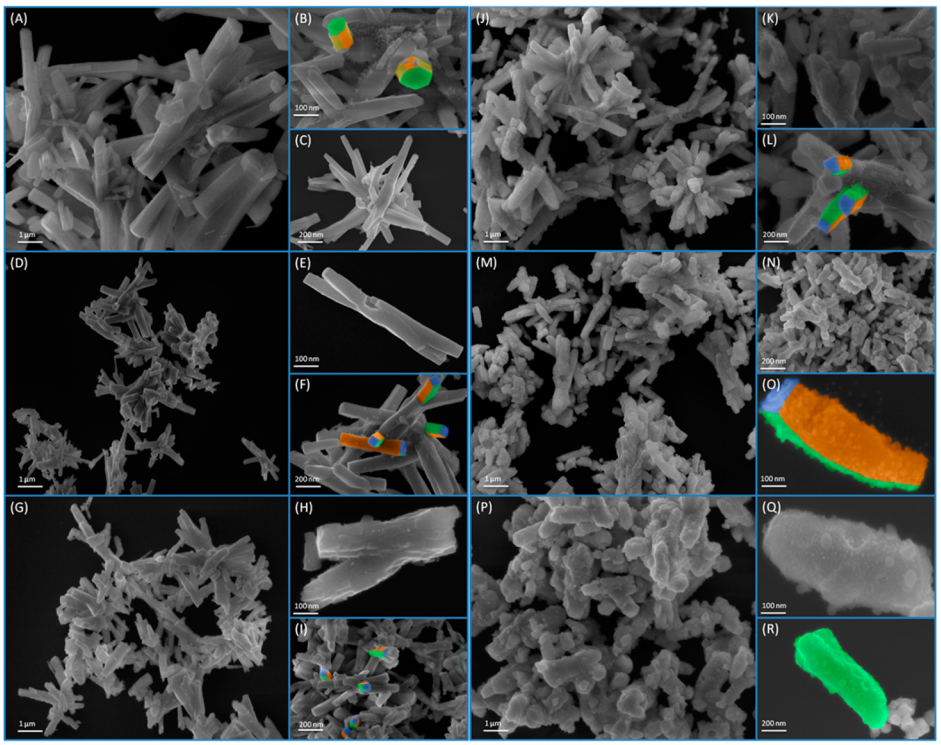

Figure 4. FEG-SEM images of α-$Ag_{2-2x}Zn_xWO_4$ (where (A–C) $x = 0$, (D–F) $x = 0.05$, (G–I) $x = 0.10$, (J–L) $x = 0.15$, (M–O) $x = 0.20$, and (P–R) $x = 0.25$) microcrystals, obtained by the CP method at 80 °C for 30 min.

FTIR Spectroscopy Analysis. FTIR data obtained in the interval of 200–1000 cm^{-1} of the α-$Ag_{2-2x}Zn_xWO_4$ (x = 0, 0.05, 0.10, 0.15, 0.20, and 0.25) microcrystals synthesized by CP at 80 °C for 30 min are displayed in Figure SI-5.

Figure SI-5a–f presents the 14 IR-active vibrational modes assigned to the $[WO_4^{2-}]$ group, Ag–O and Zn–O bonds, and Zn–O–W bond angles.

The samples exhibit two intense absorption bands at 874 and 821 cm^{-1} referring to bonds between the W–O–W and O–W–O antisymmetric stretching of the tetrahedral WO_4^{2-} group (see the inset in Figure SI-5). The 317 and 295 cm^{-1} bands represent the IR-active vibrational internal modes associated with the symmetric bending vibrations and external modes attributed to the torsional within the WO_4^{2-} group, respectively.

Figure SI-5 shows that, for the samples with $x > 0.05$, there is a change in some modes of the W–O bonds and O–W–O bending, which can be observed in the range of 400–750 cm^{-1}. This behavior is due to distortions of the $[AgO_y]$–$[WO_6]$–$[ZnO_y]$ (y = 2, 4, 6, and 7) clusters. Thus, the observed bands at 617 and 588 cm^{-1} are assigned to the bridging oxygen atoms in the W_2O_2 asymmetric stretching, with the latter related to a small shift to lower wavenumbers (cm^{-1}) for samples with x = 0.20 and 0.25 of Zn^{2+} ion substitution (see Figure SI-5e,f). The vibrations of the O–W–O moiety also results in the active modes at 737 and 926 cm^{-1}, and in the W–O–W moiety the vibrations result in the mode at 671 cm^{-1}.[47]

The absorption bands at 361 and 487 cm^{-1} can be attributed to nonsymmetric deformation modes of Zn–O bonds, and the absorption bands at 911 and 1051 cm^{-1} are related to the bending and stretching of the Zn–O–W framework.[2,70] FTIR spectra provided evidence that all α-$Ag_{2-2x}Zn_xWO_4$ powders have an orthorhombic-type structure.

FEG-SEM Morphological Analysis. Figure 4a–r presents the morphologies and microstructures of the α-$Ag_{2-2x}Zn_xWO_4$ (x = 0, 0.05, 0.10, 0.15, 0.20, and 0.25) microcrystals obtained by CP at 80 °C for 30 min.

All samples are agglomerated with a polydisperse size distribution and shape (see Figure 4a–r), in accordance with our previous studies.[3,17,47] On the basis of the Wulff construction, it is possible to find surface energy ratios to achieve the same morphologies obtained experimentaly.[54,71,72] However, this is a simple method that can be applied to show how the Zn^{2+} replacement influences the crystal morphology and, consequently, the materials properties (see Figure SI-6).

An analysis of the images for the α-Ag_2WO_4 microcrystals displayed in Figure 4a–c shows several elongated rod-like structures, and it is possible to verify that α-Ag_2WO_4 microcrystals present a well-defined face with a hexagonal shape (see Figure 4b).[3,17,47] It can be observed that some small α-Ag_2WO_4 nanocrystals, as well as large α-Ag_2WO_4 microcrystal surfaces, were not diffused within the interior. According to Cavalcante et al.,[3] this behavior is because the partial diffusion of these small microcrystals thought larger particles of α-Ag_2WO_4 and/or that thermal energy that was not enough to the normal growth rate of the α-Ag_2WO_4 microcrystals. According to Roca et al.,[17] α-Ag_2WO_4 microcrystals with a hexagonal rod-like shape have a preferential growth along the [010] direction. Coming from the vacuum structure previously obtained, the Wulff construction of the hexagonal rod-like shape can be obtained by destabilizing the (010) surface (increasing its energy) and stabilizing the (101) surface (decreasing the energy). The relative surface energies of this morphology are described in Figure SI-6b.

In the solid solution with x = 0.05 of Zn^{2+} occurs a modification in the microcrystal shapes and sizes, as can be seen in Figure 4d–f. These figures illustrate the formation of rod-like microcrystals with crystallographic face-squared shapes (see Figure 4e,f). The average size of these particles is also smaller

DOI: 10.1021/acs.inorgchem.7b00201
Inorg. Chem. XXXX, XXX, XXX–XXX

than the pure α-Ag_2WO_4. Thus, the Wulff construction of this morphology was reached destabilizing the (001) surface and stabilizing the (100) surface (see Figure SI-6c). It is worth mentioning that the elongation of these particles is provided by the decrease in the (001) surface energy in relation to the (100) and (010) surfaces. Therefore, this information allows one to know how the Zn^{2+} influences the particle growth, by providing a stabilization of the (101) surface with respect to the (100), (010), and (001) surfaces. The surface energy values in thermodynamic equilibrium can be found in Figure SI-6c.

Figure 4g–i presents the α-$Ag_{2-2x}Zn_xWO_4$ (x = 0.10) solid solution, where a similar behavior of α-$Ag_{2-2x}Zn_xWO_4$ (x = 0.05) microcrystals is observed, and this can be proved through the Wulff construction (see Figure SI-6c); however, the microcrystals show a more rugose surface and a decrease in the average size (see Figure 4h).

Figure 4j–l shows the α-$Ag_{2-2x}Zn_xWO_4$ (x = 0.15) microcrystals, which exhibit a rugose surface and face-quasi-squared shape, while also showing a curved surface (see Figure 4k,l). Finally, in the α-$Ag_{2-2x}Zn_xWO_4$ (x = 0.20 and 0.25) microcrystals the Zn^{2+} caused a pronounced change in the microcrystals' shapes and sizes (see Figures 4m,n,p–r), respectively, leading to the formation of deformed rod-like structures with curved surfaces.

In a general observation, the low concentration of Zn^{2+} initially induced the disappearance of the (101) surface at equilibrium, resulting in a tetrahedral morphology. Increasing the amount of Zn^{2+} ions, it was noticed that imperfections formed on the tetrahedral crystals, as observed in Figure 4h, up to a point where the morphologies suffered a deconfiguration (see Figure 4m–r). Therefore, the structural disorganization induced by Zn^{2+} on the lattice tends to hamper the atomic stacking at a superficial level, generating these observed changes.

Thus, Figure 5 schematizes the growth mechanism, which leads to the formation of the α-$Ag_{2-2x}Zn_xWO_4$ ($0 \le x \le 0.25$) microcrystals in comparison with FE-SEM micrographs. Initially, through the strong electrostatic attraction between the hydrated Ag^+, Zn^{2+}, and WO_4^{2-} clusters, the first nuclei are formed, and, consequently, the nucleation phase starts spontaneously with the formation of primary particles that lead the precipitation. Thus, the rapid nucleation step is followed by the uniform growth of the particles. This process is called Ostwald ripening (OR), in which the system reaches an equilibrium condition between the solubility and precipitation processes. The OR process occurs when small particles in suspension redissolve and are deposited in larger particles. This OR process can happen in two steps: a very slow or fast nucleation step, leading to the formation of polydisperse or monodisperse particles, respectively.[47,73] When a change in the morphology is observed due to the addition of Zn^{2+} clusters and to the silver vacancies, there is a spontaneous formation of oxygen vacancies in the clusters that creates irregularities or surface defects in α-$Ag_{2-2x}Zn_xWO_4$ ($0.05 \le x \le 0.25$) microcrystals, indicating a polydisperse growth nature (see the morphology in the Figure 5 inset).

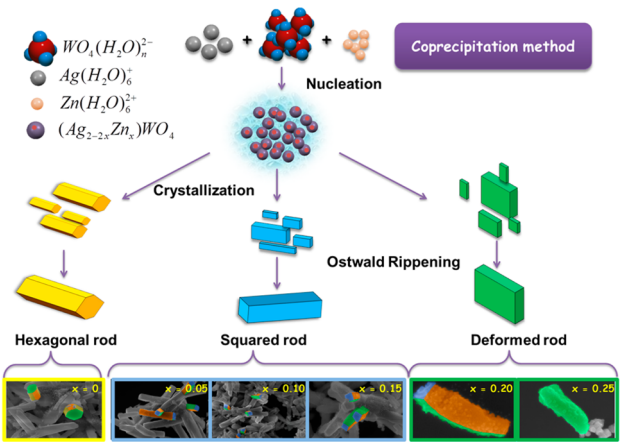

Figure 5. Schematic illustration of the proposed growth mechanism leading to the formation of α-$Ag_{2-2x}Zn_xWO_4$ ($0 \le x \le 0.25$) microcrystals.

UV–Vis Absorption Spectroscopy Analysis and Band Structures of α-$Ag_{2-2x}Zn_xWO_4$ Microcrystals. The optical band gap energies (E_{gap}) of α-$Ag_{2-2x}Zn_xWO_4$ (x = 0, 0.05, 0.10, 0.15, 0.20, and 0.25) microcrystals were calculated by the Wood-Tauc[74] method and Kubelka–Munk[75] function. The gap energy values were obtained through the equations discussed in previous works.[3,17,23,57,76] According to the literature[77,78] the α-Ag_2WO_4 microcrystals present a direct electronic transition. Additionally, on the basis of our theoretical calculations, the electronic transitions for the α-$Ag_{2-2x}Zn_xWO_4$ ($0 \le x \le 0.25$) systems are governed by an indirect transition. This information was used for the band gap energy estimation in the Wood-Tauc method.

Table 3 presents the estimated band gap values for α-$Ag_{2-2x}Zn_xWO_4$ (x = 0, 0.05, 0.10, 0.15, 0.20, and 0.25)

Table 3. Optical Band Gap Energy (E_{gap}) Values to α-$Ag_{2-2x}Zn_xWO_4$[a] Microcrystals Obtained by CP Method[b]

α-$Ag_{2-2x}Zn_xWO_4$	E_{gap} (eV)
x = 0.00	3.18
x = 0.05	3.04
x = 0.10	3.03
x = 0.15	3.07
x = 0.20	3.08
x = 0.25	3.08

[a] x = 0.00, 0.05, 0.10, 0.15, 0.20, and 0.25. [b] At 80 °C for 30 min.

microcrystals obtained by CP at 80 °C for 30 min. The UV–vis spectra of these samples are present in Figure SI-7.

As observed in Table 3, the experimental E_{gap} values show a slight decrease as the presence of Zn^{2+} ions in the α-Ag_2WO_4 lattice increases.

The study of these electronic transitions can be evaluated through theoretical calculations. Therefore, Figure 6a–c illustrates the band structures of pure α-Ag_2WO_4, for model A and model B.

Typically, the introduction of impurities in the lattice tends to decrease band gap due to the creation of new intermediate levels[3,22,57] in the forbidden region, as also observed in our model as well. This tendency can occur not only because of the insertion of impurities but also by the disordered structure as structural defects at medium range, local bond distortions,[57,68] $[WO_6]$–$[WO_6]$, $[AgO_y]$–$[AgO_y]$, or $[WO_6]$–$[AgO_y]$,[47] intrinsic surface states, and interfaces.[17]

By means of the band structure analysis, it was noticed that the pure α-Ag_2WO_4 and the two models with the Zn replacement are typically characterized by indirect electronic transitions. In the band structure of pure α-Ag_2WO_4, the top of

DOI: 10.1021/acs.inorgchem.7b00201
Inorg. Chem. XXXX, XXX, XXX–XXX

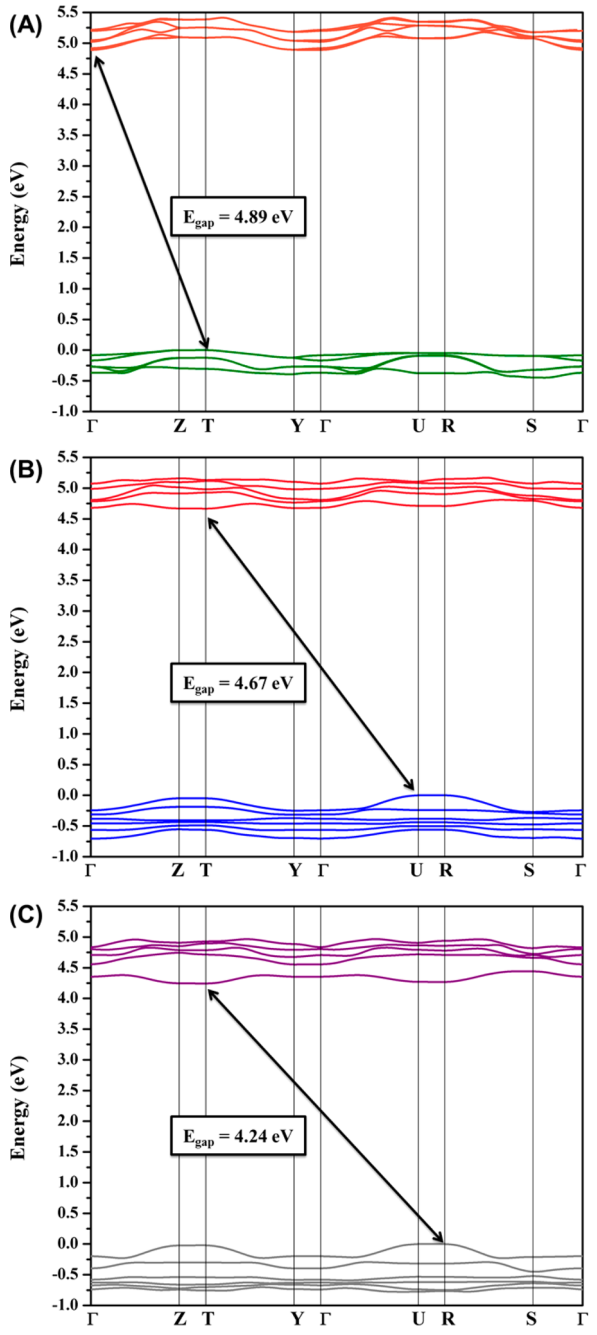

Figure 6. Band structure of (a) pure α-Ag_2WO_4, (b) model A, and (c) model B.

the valence band (VB) is located at the T point, and the bottom of the conduction band (CB) is at the Γ point; in models A and B, the bottom of the CB is located at the T point, and the top of the VB is placed at the U and R points, respectively. Even though the band gaps of the two models are similar, the indirect characteristic of the band gap was retained, although the change of U−T to R−T transition. This result confirms that the location of the replacement (in the Ag2 site in model A; in the Ag4 site in model B) affects the transition energy. The comparison between the energies revealed that model B is more stable than model A. Additionally, this stability resulted in the reduction in the band gap value due to the modification of energy levels, which can be better evaluated by the DOS analysis.

Density of States. The DOS of pure α-Ag_2WO_4 and the two models were also studied to give information in relation to the electronic transitions. Figure 7 shows the total DOS for pure α-Ag_2WO_4 and the models with Zn replacement (models A and B). For all models, the projected DOS on the W atom is principally determined in the CB with 5d orbitals. The VB is mainly resulting from the hybridization of 2p and 4d orbitals from O and Ag atoms, respectively. The Zn atoms present a

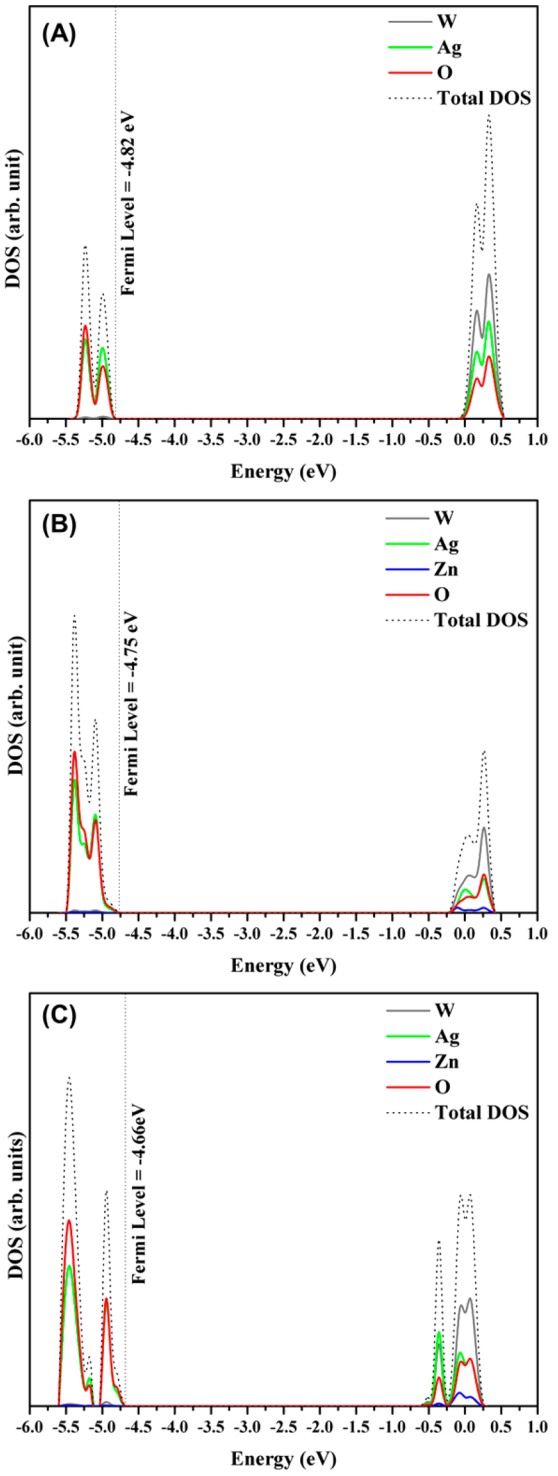

Figure 7. DOS projected in (a) pure α-Ag_2WO_4, (b) model A, and (c) model B.

DOI: 10.1021/acs.inorgchem.7b00201
Inorg. Chem. XXXX, XXX, XXX−XXX

small contribution for both bands. When we analyze these results, it is possible to notice that the region of the band gap underwent an enlargement in both bands. This fact is linked with the kinds of defects that the Zn^{2+} replacement created in the α-Ag_2WO_4 bulk.

There might be different defects in the structure; for example, shallow and deep defects. The first one is related to structural order−disorder effects, such as bond stretching or bond bending, whereas the deep defect is assigned to oxygen vacancies (V_O^x). When we induce the Zn^{2+} substitution in the theoretical models, changes in the α-Ag_2WO_4 bulk (pure model) were observed, mainly causing different types of clusters. These structural deformations and oxygen vacancies are present in $[AgO_y]$, $[ZnO_y]$ (y = 2, 4, 6, and 7), and $[WO_6]$ clusters.

Photoluminescence. PL spectra of the α-$Ag_{2-2x}Zn_xWO_4$ (x = 0, 0.05, 0.10, 0.15, 0.20, and 0.25) samples prepared by the CP method at 80 °C for 30 min with a 350.7 nm excitation are shown in Figure 8. The PL studies are an important way to evaluate the electronic levels and to analyze the theoretical models.

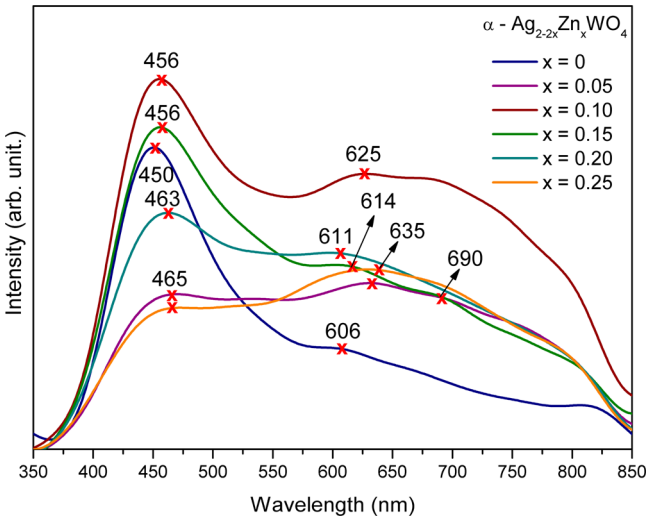

Figure 8. Emission spectra of the α-$Ag_{2-2x}Zn_xWO_4$ (x = (a) 0, (b) 0.05, (c) 0.10, (d) 0.15, (e) 0.20, and (f) 0.25) microcrystals obtained by the CP method at 80 °C for 30 min; excited at 350.7 nm with a krypton ion laser.

Figure 8 shows the PL emissions from 350 to 850 nm for all of the samples. It is possible to observe a wide band with maximum intensity emission in the violet−blue range between 450 and 465 nm and another in the orange−red region between 606 and 690 nm, related to cluster-to-cluster charge transfer processes. All spectra present a wide band in the visible range, indicating that the emission is a multilevel process,[22] involving the contribution of various energy states in the band gap.[3,68]

Figure 8 illustrates the maximum blue PL emission peak of the α-Ag_2WO_4 sample, with the maximum intensity centered at 450 nm, possibly caused by electronic transitions in the octahedral $[WO_6]$ cluster. On the one hand, a red shift to 465 nm and a decrease in the intensity are observed. On the other hand, there is an increase of the red region emission from 600 to 800 nm in the samples with the Zn^{2+} ion addition in the α-Ag_2WO_4 lattice. This red shift of the maximum emission and the changes in the PL profile of the spectra observed in Figure 8 indicate that the $[WO_6]$ and $[AgO_y]$ clusters were influenced by distortions of the $[AgO_y]$−$[WO_6]$−$[ZnO_z]$ (y = 2, 4, 6, and 7) bonds and also that there are clusters with oxygen vacancies (V_O^x). This fact can be associated with the formation of new $[ZnO_y]$ clusters in the α-Ag_2WO_4 lattice, which are responsible for the different distribution of the energy levels within the band gap,[47] confirming the substitution of Zn^{2+} on the Ag^+ site. To better understand the effect of Zn^{2+} in the α-$Ag_{2-2x}Zn_xWO_4$ lattice and its behavior on the PL properties, a deconvolution of each peak of the PL spectra was performed using the PickFit program with the Voight area function, as illustrated in Figure 9.

Figure 9 presents that, through the deconvolution of the PL spectra, four curves at λ = 441 (blue), 491 (green), 630 (red), and 768 nm (orange) were possible to cover all of the visible electromagnetic spectrum. These results show a different behavior in each sample as the concentration of Zn^{2+} in the α-$Ag_{2-2x}Zn_xWO_4$ solid solutions was increased. However, these results reveal an elevated percentage of the red and orange area, indicating a higher amount of deep defects compared to shallow defects. This behavior is different from the pure α-Ag_2WO_4 sample, which favors the blue and green area, corresponding to shallow structural defects. These oscillations in the PL emissions corroborate with the Rietveld data, which show a random distribution of Zn^{2+} ions on the Ag^+ sites. The replacement of Ag^+ by Zn^{2+} in α-$Ag_{2-2x}Zn_xWO_4$ forms a complex structure with ionic bonds and, consequently, forms complexes with strong bonds. Thus, the substitutions occur in different clusters as the number of Zn^{2+} ions are increased, causing a red shift, which is linked to the increase in the amount of deep defects. These results were confirmed by theoretical models, where it was possible to notice different clusters of $[ZnO_5{\cdot}V_O^x]$, $[ZnO_4{\cdot}2V_O^x]$, $[WO_5{\cdot}V_O^x]$, $[WO_4{\cdot}2V_O^x]$, and $[AgO_y]$ (y = 4, 5, and 6), as demonstrated in Section 3.4 (Structural Theoretical Analysis).

When the Zn^{2+} ions are doped into α-Ag_2WO_4, the red emission is favored, and it is linked to the deep defects, which are, in turn, linked to the oxygen vacancies presented in the clusters. In α-Ag_2WO_4 microcrystals, it is supposed that the Zn^{2+} ion replaces the Ag^+ ion. Thus, the replacement of bivalent ion for a monovalent requires a charge balance of the lattice.[67] This behavior is expressed through eqs 1−4.[19]

$$[WO_6]^x + [WO_5 \times V_O^x] \rightarrow [WO_6]' + [WO_5 \times V_O^\bullet] \quad (1)$$

$$2[WO_6]^x + [WO_4 \times 2V_O^x] \rightarrow 2[WO_6]' + [WO_4 \times 2V_O^\bullet] \quad (2)$$

$$[ZnO_6]^x + [ZnO_5 \times V_O^x] \rightarrow [ZnO_6]' + [ZnO_5 \times V_O^\bullet] \quad (3)$$

$$2[ZnO_6]^x + [ZnO_4 \times 2V_O^x] \rightarrow 2[ZnO_6]' + [ZnO_4 \times 2V_O^\bullet] \quad (4)$$

The oxygen vacancies can be found in different charge states in the disordered lattice, such as $[WO_5{\cdot}V_O^x]$, $[WO_4{\cdot}2V_O^x]$, $[ZnO_5{\cdot}V_O^x]$, and $[ZnO_4{\cdot}2V_O^x]$, where these donate electrons and are neutral relative to the lattice. $[WO_5{\cdot}V_O^\bullet]$, $[WO_4{\cdot}2V_O^\bullet]$, $[ZnO_5{\cdot}V_O^\bullet]$, and $[ZnO_4{\cdot}2V_O^\bullet]$ are singly ionized states and donate and capture electrons, while $[WO_5{\cdot}V_O^{\bullet\bullet}]$, $[WO_4{\cdot}2V_O^{\bullet\bullet}]$, $[ZnO_5{\cdot}V_O^{\bullet\bullet}]$, and $[ZnO_4{\cdot}V_O^{\bullet\bullet}]$ are doubly positively charged states in the lattice and capture electrons. Thus, these oxygen vacancies generate new energy states into the band gap, being attributed to $[WO_6]$, $[AgO_y]$, or $[ZnO_y]$ complex clusters.[67]

DOI: 10.1021/acs.inorgchem.7b00201
Inorg. Chem. XXXX, XXX, XXX−XXX

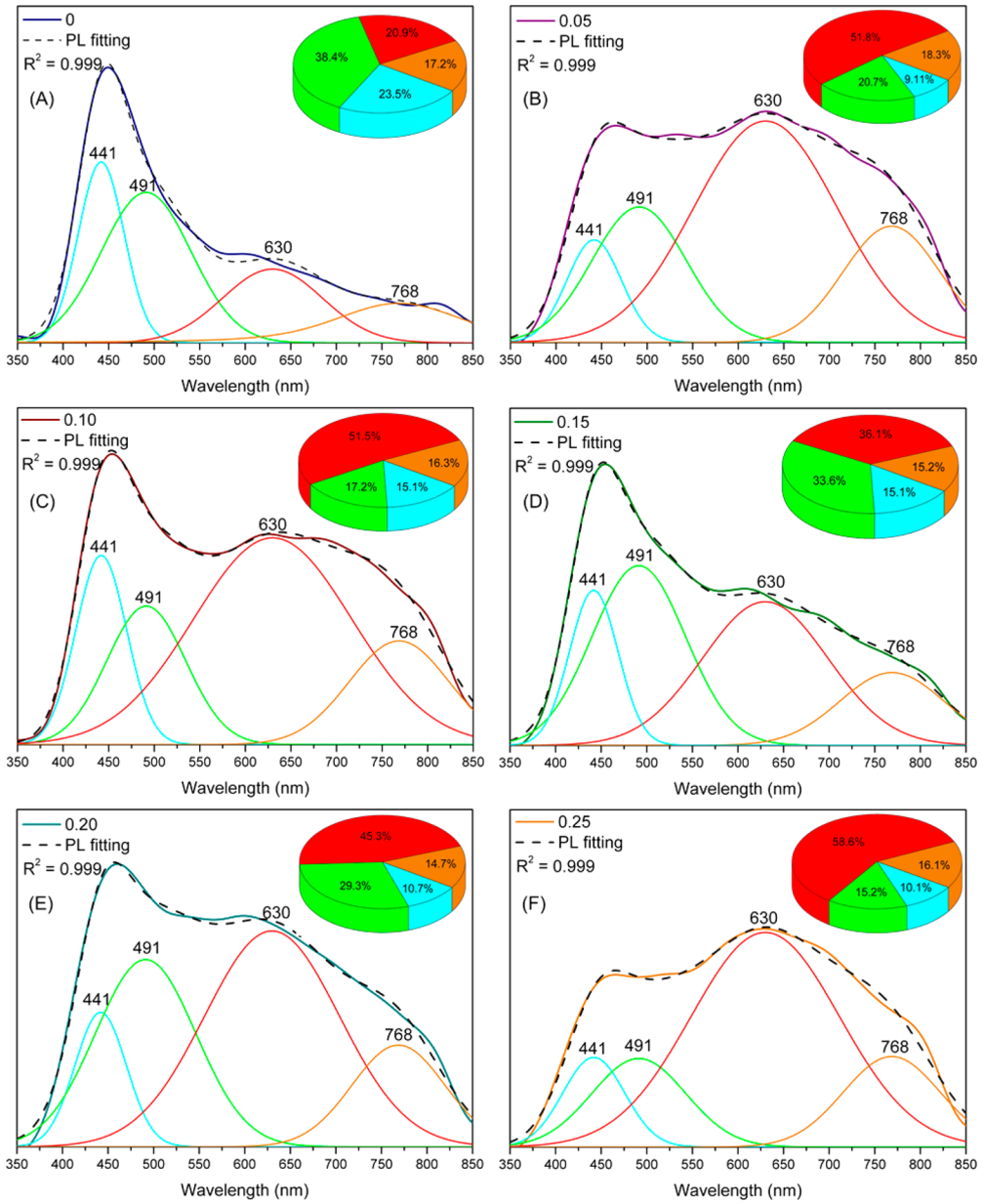

Figure 9. Deconvolution of PL spectra of α-$Ag_{2-2x}Zn_xWO_4$ (x = (a) 0, (b) 0.05, (c) 0.10, (d) 0.15, (e) 0.20, and (f) 0.25) microcrystals obtained by the CP method at 80 °C for 30 min. (insets) The area percentage of each color component corresponding to the emission peak.

However, other factors may also be involved in the PL of the α-$Ag_{2-2x}Zn_xWO_4$ samples, such as particle aggregation, differences in the size and the morphology, as well as surface characteristics.[3,57,68] Therefore, changes in the shapes and sizes of the particles are considered crucial for the variations of the luminescence emission profile. Thus, it is possible to compare the changes in the PL emission obtained in this work with the morphology of the microcrystals by increasing the amount of Zn^{2+} in the lattice (see Figures 4a–r), where significant changes in the sizes and shapes of the particles and their surfaces were observed.

4. CONCLUSIONS

In summary, α-$Ag_{2-2x}Zn_xWO_4$ ($0 \leq x \leq 0.25$) solid solutions crystals were synthesized successfully by the CP method and, for first time, the introduction of Zn^{2+} ions to control the crystal characteristics and optical properties was investigated. XRD patterns and Rietveld refinement data showed that the α-$Ag_{2-2x}Zn_xWO_4$ ($0 \leq x \leq 0.25$) microcrystals were monophasic with orthorhombic structure and space group $Pn2n$ and showed that Zn replacement occurred randomly in Ag sites in the α-Ag_2WO_4 structure, depending on the Zn concentration. Thus, structural theoretical analysis based on first-principles calculations showed that Zn replacement in α-Ag_2WO_4 structure is more favorable on the Ag4 site (tetracoordinated).

MR and FTIR spectroscopies were employed to evaluate the vibrational modes, and the results have confirmed that all vibrational modes are characteristic of the orthorhombic structure. The addition of Zn^{2+} ions in α-Ag_2WO_4 was unable to modify the stretching, torsional, and bending active vibrational modes. The theoretical values of the Raman spectra are in agreement with previously reported values and the experimental results.

DOI: 10.1021/acs.inorgchem.7b00201
Inorg. Chem. XXXX, XXX, XXX−XXX

FE-SEM images revealed that the incorporation of Zn^{2+} in the α-Ag_2WO_4 structure affected the shape and size of the microcrystals. On the basis of the Wulff's theorem and theoretical results, a model was elaborated to determine the surface energies of the α-Ag_2WO_4 crystals with atomic-level resolution and the crystal morphologies at equilibrium. Particle shape transformations of the α-Ag_2WO_4 were estimated by controlling the ratio between surface energy values of each face. The Ag substitution by Zn decreased the number of exposed surfaces, and the shape changed from roll-like to curved surfaces in α-Ag_2WO_4 and α-$Ag_{2-2x}Zn_xWO_4$ (x = 0.25), respectively.

The UV−vis spectrum indicated that, for α-Ag_2WO_4 microcrystals and α-$Ag_{2-2x}Zn_xWO_4$, the band gap value was governed by an indirect transition. The PL behavior of the α-Ag_2WO_4 microcrystals was associated with structural rearrangements, provoked by the order−disorder effects on $[WO_6]^x_o$−$[WO_6]^x_d$ and $[AgO_y]^x_o$−$[AgO_y]^x_d$ (y = 2, 4, 6, and 7) clusters. These effects are linked to shallow defects, resulting in a higher percentage of the blue region contribution in the PL profile. In the α-$Ag_{2-2x}Zn_xWO_4$ ($0.05 \le x \le 0.25$) microcrystals, the PL is associated with distortion and oxygen vacancies (V_O^x) in these clusters causing a red shift, which is linked to an increase in the amount of deep defects.

■ ASSOCIATED CONTENT

Supporting Information

The Supporting Information is available free of charge on the ACS Publications website at DOI: 10.1021/acs.inorgchem.7b00201.

Photoluminescence. X-ray fluorescence. Lattice parameters, unit cell volume and statistical parameters. Atomic positions. Raman modes (in cm^{-1}) compared to the literature. XRD. Theoretical models. FTIR spectra. Map of morphologies. UV−vis spectra for α-$Ag_{2-2x}Zn_xWO_4$ ($0 \le x \le 0.25$) samples (PDF)

Accession Codes

CCDC 1550814, 1550819, 1550824−1550826, and 1550966 contain the supplementary crystallographic data for this paper. These data can be obtained free of charge via www.ccdc.cam.ac.uk/data_request/cif, or by emailing data_request@ccdc.cam.ac.uk, or by contacting The Cambridge Crystallographic Data Centre, 12 Union Road, Cambridge CB2 1EZ, UK; fax: +44 1223 336033.

■ AUTHOR INFORMATION

Corresponding Author

*E-mail: andres@qfa.uji.es.

ORCID

Paula F. S. Pereira: 0000-0002-1335-1331

Julio R. Sambrano: 0000-0002-5217-7145

Juan Andrés: 0000-0003-0232-3957

Notes

The authors declare no competing financial interest.

■ ACKNOWLEDGMENTS

This work was financially supported by Fundação de Amparo à Pesquisa do Estado de São Paulo (FAPESP 2012/14004-5, 2013/07296-2, 2013/26671-9, 2013/23995-8, 2014/14171-4, and 2016/07476-9), Conselho Nacional de Desenvolvimento Científico e Tecnológico (CNPq; 46126-4, 479644/2012-8, 350711/2012-7, 304531/2013-8, and 151136/2013-0). Coordenação de Aperfeiçoamento de Pessoal de Nível Superior (CAPES, 787027/2013, and 8881068492/2014-01). The computational facilities were supported by resources supplied by Molecular Simulations Laboratory, São Paulo State University Bauru, Brazil. J.A. is grateful to Generalitat Valenciana for PrometeoII/2014/022, ACOMP/2014/270, and ACOMP/2015/1202 projects, Ministerio de Economia y Competitividad (Spain), for CTQ2015-65207-P project, and Programa de Cooperación Científica con Iberoamerica (Brasil) of Ministerio de Educación (Spanish Brazilian program PHBP14-00020), J.A. acknowledges Ministerio de Economia y Competitividad, "Salvador Madariaga" program, PRX15/00261.

■ REFERENCES

(1) da Silva, L. F.; Catto, A. C.; Avansi, W.; Cavalcante, L. S.; Mastelaro, V. R.; Andres, J.; Aguir, K.; Longo, E. Acetone gas sensor based on alpha-Ag2WO4 nanorods obtained via a microwave-assisted hydrothermal route. *J. Alloys Compd.* **2016**, *683*, 186−190.

(2) Amouzegar, Z.; Naghizadeh, R.; Rezaie, H. R.; Ghahari, M.; Aminzare, M. Cubic ZnWO4 nano-photocatalysts synthesized by the microwave-assisted precipitation technique. *Ceram. Int.* **2015**, *41*, 1743−1747.

(3) Cavalcante, L. S.; Almeida, M. A.; Avansi, W., Jr.; Tranquilin, R. L.; Longo, E.; Batista, N. C.; Mastelaro, V. R.; Li, M. S. Cluster coordination and photoluminescence properties of alpha-Ag2WO4 microcrystals. *Inorg. Chem.* **2012**, *51*, 10675−87.

(4) Chen, H.; Xu, Y. Photoactivity and stability of Ag2WO4 for organic degradation in aqueous suspensions. *Appl. Surf. Sci.* **2014**, *319*, 319−323.

(5) Longo, V. M.; De Foggi, C. C.; Ferrer, M. M.; Gouveia, A. F.; Andre, R. S.; Avansi, W.; Vergani, C. E.; Machado, A. L.; Andres, J.; Cavalcante, L. S.; Hernandes, A. C.; Longo, E. Potentiated Electron Transference in alpha-Ag2WO4Microcrystals with Ag Nanofilaments as Microbial Agent. *J. Phys. Chem. A* **2014**, *118*, 5769−5778.

(6) Bian, T.; Shang, L.; Yu, H. J.; Perez, M. T.; Wu, L. Z.; Tung, C. H.; Nie, Z. H.; Tang, Z. Y.; Zhang, T. R. Spontaneous Organization of Inorganic Nanoparticles into Nanovesicles Triggered by UV Light. *Adv. Mater.* **2014**, *26*, 5613−5618.

(7) Niu, L. Y.; Li, Z. P.; Xu, Y.; Sun, J. F.; Hong, W.; Liu, X. H.; Wang, J. Q.; Yang, S. R. Simple Synthesis of Amorphous NiWO4 Nanostructure and Its Application as a Novel Cathode Material for Asymmetric Supercapacitors. *ACS Appl. Mater. Interfaces* **2013**, *5*, 8044−8052.

(8) Pourmortazavi, S. M.; Rahimi-Nasrabadi, M.; Khalilian-Shalamzari, M.; Zahedi, M. M.; Hajimirsadeghi, S. S.; Omrani, I. Synthesis, structure characterization and catalytic activity of nickel tungstate nanoparticles. *Appl. Surf. Sci.* **2012**, *263*, 745−752.

(9) Shang, L.; Zhou, C.; Bian, T.; Yu, H. J.; Wu, L. Z.; Tung, C. H.; Zhang, T. R. Facile synthesis of hierarchical ZnIn2S4 submicrospheres composed of ultrathin mesoporous nanosheets as a highly efficient visible-light-driven photocatalyst for H-2 production. *J. Mater. Chem. A* **2013**, *1*, 4552−4558.

(10) Wei, H. G.; Ding, D. W.; Yan, X. R.; Guo, J.; Shao, L.; Chen, H. R.; Sun, L. Y.; Colorado, H. A.; Wei, S. Y.; Guo, Z. H. Tungsten Trioxide/Zinc Tungstate Bilayers: Electrochromic Behaviors, Energy Storage and Electron Transfer. *Electrochim. Acta* **2014**, *132*, 58−66.

(11) Yourey, J. E.; Pyper, K. J.; Kurtz, J. B.; Bartlett, B. M. Chemical Stability of CuWO4 for Photoelectrochemical Water Oxidation. *J. Phys. Chem. C* **2013**, *117*, 8708−8718.

(12) Zhang, D. H.; Zhou, C.; Sun, Z. H.; Wu, L. Z.; Tung, C. H.; Zhang, T. R. Magnetically recyclable nanocatalysts (MRNCs): a versatile integration of high catalytic activity and facile recovery. *Nanoscale* **2012**, *4*, 6244−6255.

(13) Ramezani, M.; Pourmortazavi, S. M.; Sadeghpur, M.; Yazdani, A.; Kohsari, I. Silver tungstate nanostructures: electrochemical

DOI: 10.1021/acs.inorgchem.7b00201
Inorg. Chem. XXXX, XXX, XXX−XXX

synthesis and its statistical optimization. *J. Mater. Sci.: Mater. Electron.* **2015**, *26*, 3861−3867.
(14) Dutta, D. P.; Singh, A.; Ballal, A.; Tyagi, A. K. High Adsorption Capacity for Cationic Dye Removal and Antibacterial Properties of Sonochemically Synthesized Ag2WO4 Nanorods. *Eur. J. Inorg. Chem.* **2014**, *2014*, 5724−5732.
(15) Wang, Q. P.; Guo, X. X.; Wu, W. H.; Liu, S. X. Preparation of Fine Ag2WO4 Antibacterial Powders and Its Application in the Sanitary Ceramics. *Adv. Mater. Res.* **2011**, *284-286*, 1321−1325.
(16) De Santana, Y. V. B.; Gomes, J. E. C.; Matos, L.; Cruvinel, G. H.; Perrin, A.; Perrin, C.; Andres, J.; Varela, J. A.; Longo, E. Silver Molybdate and Silver Tungstate Nanocomposites with Enhanced Photoluminescence. *Nanomater. Nanotechnol.* **2014**, *4*, 22.
(17) Roca, R. A.; Sczancoski, J. C.; Nogueira, I. C.; Fabbro, M. T.; Alves, H. C.; Gracia, L.; Santos, L. P. S.; de Sousa, C. P.; Andres, J.; Luz, G. E., Jr.; Longo, E.; Cavalcante, L. S. Facet-dependent photocatalytic and antibacterial properties of alpha-Ag2WO4 crystals: combining experimental data and theoretical insights. *Catal. Sci. Technol.* **2015**, *5*, 4091−4107.
(18) Zhang, R.; Cui, H.; Yang, X.; Liu, H.; Tang, H.; Li, Y. Facile hydrothermal synthesis and photocatalytic activity of rod-like nano-sized silver tungstate. *Micro Nano Lett.* **2012**, *7*, 1285−1288.
(19) da Silva, L. F.; Catto, A. C.; Avansi, W., Jr.; Cavalcante, L. S.; Andres, J.; Aguir, K.; Mastelaro, V. R.; Longo, E. A novel ozone gas sensor based on one-dimensional (1D) alpha-Ag2WO4 nanostructures. *Nanoscale* **2014**, *6*, 4058−4062.
(20) Longo, E.; Cavalcante, L. S.; Volanti, D. P.; Gouveia, A. F.; Longo, V. M.; Varela, J. A.; Orlandi, M. O.; Andres, J. Direct in situ observation of the electron-driven synthesis of Ag filaments on alpha-Ag2WO4 crystals. *Sci. Rep.* **2013**, *3*, 1676.
(21) Cui, X. J.; Yu, S. H.; Li, L. L.; Biao, L.; Li, H. B.; Mo, M. S.; Liu, X. M. Selective synthesis and characterization of single-crystal silver molybdate/tungstate nanowires by a hydrothermal process. *Chem. - Eur. J.* **2004**, *10*, 218−223.
(22) Sreedevi, A.; Priyanka, K. P.; Babitha, K. K.; Aloysius Sabu, N.; Anu, T. S.; Varghese, T. Chemical synthesis, structural characterization and optical properties of nanophase α-Ag2WO4. *Indian J. Phys.* **2015**, *89*, 889−897.
(23) Pinatti, I. M.; Nogueira, I. C.; Pereira, W. S.; Pereira, P. F. S.; Gonçalves, R. F.; Varela, J. A.; Longo, E.; Rosa, I. L. V. Structural and Photoluminescence Properties of Eu3+ Doped α-Ag2WO4 Synthesized by the Green Coprecipitation Methodology. *Dalton Trans.* **2015**, *44*, 17673−17685.
(24) Vafaeezadeh, M.; Hashemi, M. M. One pot oxidative cleavage of cyclohexene to adipic acid using silver tungstate nano-rods in a Bronsted acidic ionic liquid. *RSC Adv.* **2015**, *5*, 31298−31302.
(25) Pan, L.; Li, L.; Chen, Y. Synthesis and electrocatalytic properties of microsized Ag2WO4 and nanoscaled MWO4 (M = Co, Mn). *J. Sol-Gel Sci. Technol.* **2013**, *66*, 330−336.
(26) Li, J.; Yu, C.; Zheng, C.; Etogo, A.; Xie, Y.; Zhong, Y.; Hu, Y. Facile formation of Ag2WO4/AgX (X= Cl, Br, I) hybrid nanorods with enhanced visible-light-driven photoelectrochemical properties. *Mater. Res. Bull.* **2015**, *61*, 315−320.
(27) Wang, X.; Fu, C.; Wang, P.; Yu, H.; Yu, J. Hierarchically porous metastable beta-Ag2WO4 hollow nanospheres: controlled synthesis and high photocatalytic activity. *Nanotechnology* **2013**, *24*, 165602.
(28) Pereira, W. d. S.; Andres, J.; Gracia, L.; San-Miguel, M. A.; da Silva, E. Z.; Longo, E.; Longo, V. M. Elucidating the real-time Ag nanoparticle growth on alpha-Ag2WO4 during electron beam irradiation: experimental evidence and theoretical insights. *Phys. Chem. Chem. Phys.* **2015**, *17*, 5352−5359.
(29) George, T.; Joseph, S.; Mathew, S. Synthesis and characterization of nanophased silver tungstate. *Pramana* **2005**, *65*, 793−799.
(30) Zhu, J.; Fan, H.; Sun, J.; Ai, S. Anion-exchange precipitation synthesis of a-Ag2WO4/Zn−Cr layered double hydroxides composite with enhanced visible-light-driven photocatalytic activity. *Sep. Purif. Technol.* **2013**, *120*, 134−140.
(31) Ng, C. H. B.; Fan, W. Y. Preparation of highly uniform 1-dimensional alpha-Ag2WO4 nanostructures with controllable aspect ratio and study of the growth mechanism. *CrystEngComm* **2016**, *18*, 8010−8019.
(32) Song, Q.-W.; Yu, B.; Li, X.-D.; Ma, R.; Diao, Z.-F.; Li, R.-G.; Li, W.; He, L.-N. Efficient chemical fixation of CO2 promoted by a bifunctional Ag2WO4/Ph3P system. *Green Chem.* **2014**, *16*, 1633.
(33) Guo, C.-X.; Yu, B.; Xie, J.-N.; He, L.-N. Silver tungstate: a single-component bifunctional catalyst for carboxylation of terminal alkynes with CO2 in ambient conditions. *Green Chem.* **2015**, *17*, 474−479.
(34) Lin, Z.; Li, J.; Zheng, Z.; Yan, J.; Liu, P.; Wang, C.; Yang, G. Electronic Reconstruction of alpha-Ag2WO4 Nanorods for Visible-Light Photocatalysis. *ACS Nano* **2015**, *9*, 7256−7265.
(35) Cheng, L.; Shao, Q.; Shao, M.; Wei, X.; Wu, Z. Photoswitches of One-Dimensional Ag2MO4 (M = Cr, Mo, and W). *J. Phys. Chem. C* **2009**, *113*, 1764−1768.
(36) Hallaoui, A.; Taoufyq, A.; Arab, M.; Bakiz, B.; Benlhachemi, A.; Bazzi, L.; Villain, S.; Valmalette, J. C.; Guinneton, F.; Gavarri, J. R. Influence of chemical substitution on the photoluminescence of Sr(1-x)PbxWO4 solid solution. *J. Solid State Chem.* **2015**, *227*, 186−195.
(37) Culver, S. P.; Greaney, M. J.; Tinoco, A.; Brutchey, R. L. Low-temperature synthesis of homogeneous solid solutions of scheelite-structured Ca1-xSrxWO4 and Sr1-xBaxWO4 nanocrystals. *Dalton Trans.* **2015**, *44*, 15042−15048.
(38) Priya, A.; Sinha, E.; Rout, S. K. Structural, optical and microwave dielectric properties of Ba1-xSrxWO4 ceramics prepared by solid state reaction route. *Solid State Sci.* **2013**, *20*, 40−45.
(39) Porto, S. L.; Longo, E.; Pizani, P. S.; Boschi, T. M.; Simoes, L. G. P.; Lima, S. J. G.; Ferreira, J. M.; Soledade, L. E. B.; Espinoza, J. W. M.; Cassia-Santos, M. R.; Maurera, M.; Paskocimas, C. A.; Santos, I. M. G.; Souza, A. G. Photoluminescence in the CaXSr1-xWO4 system at room temperature. *J. Solid State Chem.* **2008**, *181*, 1876−1881.
(40) Taoufyq, A.; Mauroy, V.; Guinneton, F.; Bakiz, B.; Villain, S.; Hallaoui, A.; Benlhachemi, A.; Nolibe, G.; Lyoussi, A.; Gavarri, J. R. Role of the chemical substitution on the luminescence properties of solid solutions Ca(l-x)Cd(x)WO4 ($0 \le x \le 1$). *Mater. Res. Bull.* **2015**, *70*, 40−46.
(41) Huang, H. W.; Liu, L. Y.; Tian, N.; Zhang, Y. H. Structure, optical properties, and magnetism of Zn1-xNixWO4 ($0 \le x \le 1$) solid solution. *J. Alloys Compd.* **2015**, *637*, 471−475.
(42) Patureau, P.; Josse, M.; Dessapt, R.; Mevellec, J. Y.; Porcher, F.; Maglione, M.; Deniard, P.; Payen, C. Incorporation of Jahn-Teller Cu2+ Ions into Magnetoelectric Multiferroic MnWO4: Structural, Magnetic, and Dielectric Permittivity Properties of Mn1-xCuxWO4 ($x \le 0.25$). *Inorg. Chem.* **2015**, *54*, 10623−10631.
(43) Zhang, J. F.; Pan, J. G.; Yin, J.; Wang, J.; Pan, J. G.; Chen, H. B.; Mao, R. H. Structural investigation and scintillation properties of Cd1-xZnxWO4 solid solution single crystals. *CrystEngComm* **2015**, *17*, 3503−3508.
(44) Siritanon, T.; Jiamprasertboon, A.; Yong, N. Structure and optical properties of Ni1-xCoxWO4 solid solutions. *Mater. Lett.* **2015**, *145*, 316−320.
(45) Yourey, J. E.; Kurtz, J. B.; Bartlett, B. M. Structure, Optical Properties, and Magnetism of the Full Zn1-xCuxWO4 ($0 \le x \le 1$) Composition Range. *Inorg. Chem.* **2012**, *51*, 10394−10401.
(46) Han, S. L.; Xiao, K.; Liu, L. Y.; Huang, H. W. Zn1-xCoxWO4 ($0 \le x \le 1$) full range solid solution: Structure, optical properties, and magnetism. *Mater. Res. Bull.* **2016**, *74*, 436−440.
(47) Pereira, W. d. S.; Ferrer, M. M.; Botelho, G.; Gracia, L.; Nogueira, I. C.; Pinatti, I. M.; Rosa, I. L. V.; La Porta, F. d. A.; Andrés, J.; Longo, E. Effects of chemical substitution on the structural and optical properties of α-Ag2−2xNixWO4 ($0 \le x \le 0.08$) solid solutions. *Phys. Chem. Chem. Phys.* **2016**, *18*, 21966−21975.
(48) Andres, J.; Gracia, L.; Gonzalez-Navarrete, P.; Longo, V. M.; Avansi, W., Jr.; Volanti, D. P.; Ferrer, M. M.; Lemos, P. S.; La Porta, F. A.; Hernandes, A. C.; Longo, E. Structural and electronic analysis of the atomic scale nucleation of Ag on alpha-Ag2WO4 induced by electron irradiation. *Sci. Rep.* **2015**, *4*, 5391.

DOI: 10.1021/acs.inorgchem.7b00201
Inorg. Chem. XXXX, XXX, XXX−XXX

(49) Schofield, P. F.; Knight, K. S.; Cressey, G. Neutron powder diffraction study of the scintillator material ZnWO4. *J. Mater. Sci.* **1996**, *31*, 2873−2877.
(50) Dovesi, R.; Saunders, V. R.; Roetti, C.; Orlando, R.; Zicovich-Wilson, C. M.; Pascale, F.; Civalleri, B.; Doll, K.; Harrison, N. M.; Bush, I. J.; D'Arco, P.; Llunel, M.; Causà, M.; Noël, Y. *CRYSTAL14 User's Manual;* Theoretical Chemistry Group: University of Turin: Italy, 2014.
(51) Becke, A. D. Density-Functional Thermochemistry 0.3. The Role of Exact Exchange. *J. Chem. Phys.* **1993**, *98*, 5648−5652.
(52) Lee, C. T.; Yang, W. T.; Parr, R. G. Development of the Colle-Salvetti Correlation-Energy Formula into a Functional of the Electron-Density. *Phys. Rev. B: Condens. Matter Mater. Phys.* **1988**, *37*, 785−789.
(53) Crystal, Basis Sets Library. http://www.crystal.unito.it/Basis_Sets/Ptable.html.
(54) Andrés, J.; Gracia, L.; Gouveia, A. F.; Ferrer, M. M.; Longo, E. Effects of surface stability on the morphological transformation of metals and metal oxides as investigated by first-principles calculations. *Nanotechnology* **2015**, *26*, 405703−405713.
(55) Skarstad, P. M.; Geller, S. W4016)8- Polyion in the high temperature modification of silver tungstate. *Mater. Res. Bull.* **1975**, *10*, 791−800.
(56) Turkovic, A.; Fox, D. L.; Scott, J. F.; Geller, S.; Ruse, G. F. High temperature raman spectroscopy of silver tetratungstate, Ag8W4016. *Mater. Res. Bull.* **1977**, *12*, 189−196.
(57) Gouveia, A. F.; Sczancoski, J. C.; Ferrer, M. M.; Lima, A. S.; Santos, M. R.; Li, M. S.; Santos, R. S.; Longo, E.; Cavalcante, L. S. Experimental and theoretical investigations of electronic structure and photoluminescence properties of beta-Ag2MoO4 microcrystals. *Inorg. Chem.* **2014**, *53*, 5589−99.
(58) Larson, A. C.; Von Dreele, R. B. GSAS. *Gem. Struc. Anal. Syst.* **2004**, 1−224.
(59) Rietveld, H. M. A profile refinement method for nuclear and magnetic structures. *J. Appl. Crystallogr.* **1969**, *2*, 65−71.
(60) Thompson, P.; Cox, D. E.; Hastings, J. B. Rietveld Refinement of Debye-Scherrer Synchrotron X-ray Data from Al2O3. *J. Appl. Crystallogr.* **1987**, *20*, 79−83.
(61) Finger, L. W.; Cox, D. E.; Jephcoat, A. P. A correction for powder diffraction peak asymmetry due to axial divergence. *J. Appl. Crystallogr.* **1994**, *27*, 892−900.
(62) Stephens, P. W. Phenomenological model of anisotropic peak broadening in powder diffraction. *J. Appl. Crystallogr.* **1999**, *32*, 281−289.
(63) Momma, K.; Izumi, F. VESTA 3for three-dimensional visualization of crystal, volumetric and morphology data. *J. Appl. Crystallogr.* **2011**, *44*, 1272−1276.
(64) Cavalcante, L. S.; Sczancoski, J. C.; Espinosa, J. W. M.; Varela, J. A.; Pizani, P. S.; Longo, E. Photoluminescent behavior of BaWO4 powders processed in microwave-hydrothermal. *J. Alloys Compd.* **2009**, *474*, 195−200.
(65) Guo, C.; Chen, T.; Luan, L.; Zhang, W.; Huang, D. Luminescent properties of R2(MoO4)3:Eu3+ (R = La, Y, Gd) phosphors prepared by sol−gel process. *J. Phys. Chem. Solids* **2008**, *69*, 1905−1911.
(66) Cavalcante, L. S.; Sczancoski, J. C.; Albarici, V. C.; Matos, J. M. E.; Varela, J. A.; Longo, E. Synthesis, characterization, structural refinement and optical absorption behavior of PbWO4 powders. *Mater. Sci. Eng., B* **2008**, *150*, 18−25.
(67) Pereira, P. F. S.; de Moura, A. P.; Nogueira, I. C.; Lima, M. V. S.; Longo, E.; de Sousa Filho, P. C.; Serra, O. A.; Nassar, E. J.; Rosa, I. L. V. Study of the annealing temperature effect on the structural and luminescent properties of SrWO4:Eu phosphors prepared by a non-hydrolytic sol-gel process. *J. Alloys Compd.* **2012**, *526*, 11−21.
(68) Longo, E.; Volanti, D. P.; Longo, V. M.; Gracia, L.; Nogueira, I. C.; Almeida, M. A. P.; Pinheiro, A. N.; Ferrer, M. M.; Cavalcante, L. S.; Andres, J. Toward an Understanding of the Growth of Ag Filaments on alpha-Ag2WO4 and Their Photoluminescent Properties: A Combined Experimental and Theoretical Study. *J. Phys. Chem. C* **2014**, *118*, 1229−1239.
(69) Sczancoski, J. C.; Cavalcante, L. S.; Joya, M. R.; Espinosa, J. W.; Pizani, P. S.; Varela, J. A.; Longo, E. Synthesis, growth process and photoluminescence properties of SrWO4 powders. *J. Colloid Interface Sci.* **2009**, *330*, 227−36.
(70) Keereeta, Y.; Thongtem, S.; Thongtem, T. Enhanced photocatalytic degradation of methylene blue by WO3/ZnWO4 composites synthesized by a combination of microwave-solvothermal method and incipient wetness procedure. *Powder Technol.* **2015**, *284*, 85−94.
(71) Gouveia, A. F.; Ferrer, M. M.; Sambrano, J. R.; Andres, J.; Longo, E. Modeling the atomic-scale structure, stability, and morphological transformations in the tetragonal phase of LaVO4. *Chem. Phys. Lett.* **2016**, *660*, 87−92.
(72) Ferrer, M. M.; Gouveia, A. F.; Gracia, L.; Longo, E.; Andres, J. A 3D platform for the morphology modulation of materials: First principles calculations on the thermodynamic stability and surface structure of metal oxides: Co3O4, α-Fe2O3, and In2O3. *Modell. Simul. Mater. Sci. Eng.* **2016**, *24*, 025007−025016.
(73) de Sousa Filho, P. C.; Serra, O. A. Liquid phase synthesis methodologies for the obtainment of rare earth-based inorganic nanomaterials. *Quim. Nova* **2015**, *38*, 679−U259.
(74) Wood, D. L.; Tauc, J. Weak Absorption Tails in Amorphous Semiconductors. *Phys. Rev. B* **1972**, *5*, 3144−3151.
(75) Kubelka, P.; Munk, F. Ein Beitrag Zur Optik Der Farbanstriche. *Zeit. Fur. Technol. Physik* **1931**, *12*, 593−601.
(76) Pereira, P. F. S.; Nogueira, I. C.; Longo, E.; Nassar, E. J.; Rosa, I. L. V.; Cavalcante, L. S. Rietveld refinement and optical properties of SrWO4:Eu3+ powders prepared by the non-hydrolytic sol-gel method. *J. Rare Earths* **2015**, *33*, 113−128.
(77) Tang, J. W.; Ye, J. H. Correlation of crystal structures and electronic structures and photocatalytic properties of the W-containing oxides. *J. Mater. Chem.* **2005**, *15*, 4246−4251.
(78) Kim, D. W.; Cho, I.-S.; Lee, S.; Bae, S.-T.; Shin, S. S.; Han, G. S.; Jung, H. S.; Hong, K. S. Photophysical and Photocatalytic Properties of Ag2M2O7 (M = Mo, W). *J. Am. Ceram. Soc.* **2010**, *93*, 3867−3872.

DOI: 10.1021/acs.inorgchem.7b00201
Inorg. Chem. XXXX, XXX, XXX−XXX